Novel allosteric ligands of the angiotensin receptor AT1R as autoantibody blockers

Khuraijam Dhanachandra Singh[a], Zaira P. Jara[a], Terri Harford[a], Prasenjit Prasad Saha[a], Triveni R. Pardhi[a], Russell Desnoyer[a], and Sadashiva S. Karnik[a,1]

[a]Department of Cardiovascular and Metabolic Sciences, Cleveland Clinic Lerner College of Medicine at Case Western Reserve University, Cleveland, OH 44195

Edited by Robert J. Lefkowitz, HHMI, Durham, NC, and approved June 11, 2021 (received for review September 10, 2020)

While orthosteric ligands of the angiotensin II (AngII) type 1 receptor (AT1R) are available for clinical and research applications, allosteric ligands are not known for this important G protein-coupled receptor (GPCR). Allosteric ligands are useful tools to modulate receptor pharmacology and subtype selectivity. Here, we report AT1R allosteric ligands for a potential application to block autoimmune antibodies. The epitope of autoantibodies for AT1R is outside the orthosteric pocket in the extracellular loop 2. A molecular dynamics simulation study of AT1R structure reveals the presence of a druggable allosteric pocket encompassing the autoantibody epitope. Small molecule binders were then identified for this pocket using structure-based high-throughput virtual screening. The top 18 hits obtained inhibited the binding of antibody to AT1R and modulated agonist-induced calcium response of AT1R. Two compounds out of 18 studied in detail exerted a negative allosteric modulator effect on the functions of the natural agonist AngII. They blocked antibody-enhanced calcium response and reactive oxygen species production in vascular smooth muscle cells as well as AngII-induced constriction of blood vessels, demonstrating their efficacy in vivo. Our study thus demonstrates the feasibility of discovering inhibitors of the disease-causing autoantibodies for GPCRs. Specifically, for AT1R, we anticipate development of more potent allosteric drug candidates for intervention in autoimmune maladies such as preeclampsia, bilateral adrenal hyperplasia, and the rejection of organ transplants.

allosteric ligand | angiotensin | autoantibody | AT1R | GPCRs

Among diseases linked to G protein-coupled receptors (GPCRs), dysregulation by an autoimmune antibody is reported for many GPCRs with no autoantibody blocking drugs available (1, 2). Well-known examples include Graves' disease with anti-thyrotropin receptor antibodies, congestive heart failure in Chagas disease because of anti–β_1-adrenergic receptor antibodies, and cardiomyopathies because of autoantibodies against α1-, β_1- and β_2- adrenergic receptors. Chronic neurological disorders associated with antibodies against mGluRs, GABA receptors, serotonin receptors, calcium sensing GPCR, and muscarinic M1 and M2 receptors are documented. Autoantibodies directed against the angiotensin II (AngII) type 1 receptor (AT1R) cause preeclampsia in women, which causes mortalities of mother and fetus if the pregnancy is not prematurely terminated medically (3, 4). Preeclampsia accounts for 295,000 annual deaths globally, with estimated incidence of 1 in 25 pregnancies in the United States, 1 in 10 pregnancies in Asia, and one-quarter of all maternal deaths in Latin America (5, 6). Autoantibodies are produced in both genders and have been linked to adrenal hyperplasia, hyper-aldosteronism, the rejection of organ transplants, and vasculopathy (7, 8).

Empirical evidence suggests that GPCR-directed autoantibodies enhance cellular signaling responsible for the disease (Fig. 1*A*). In preeclampsia, AT1R signaling through Gq-mediated calcium release and the production of reactive oxygen species (ROS) is involved (4–8). Since existing AT1R-blockers (ARBs) or angiotensin-converting enzyme inhibitors (ACEi) are contraindicated in pregnancy because of a potential reduction in fetoplacental circulation causing fetopathy, they are not used in treatments for autoimmune preeclampsia (9).

Canonical ligand action models conceptualize the induction of active state as the physiological basis of AngII function and induction of inactive state as the therapeutic basis of ARBs when they bind to the AT1R orthosteric pocket (10–15). Crystal structures of AT1R bound to agonist AngII-, β-arrestin–biased agonist sAngII- (Sar^1, Ile^8-AngII), and antihypertensive antagonist ARBs have validated active and inactive states of AT1R in which the configuration of critical residues and motifs change (10, 12–14). The autoantibody-binding ECL2 is not part of the orthosteric pocket, and the mechanism of hyperactivation of AT1R in preeclampsia may be distinct. The epitope sequence for binding IgGs from autoimmune patients is –AFHYESQ– (*SI Appendix*, Fig. S1*A*) residues 181 to 187 in the ECL2 (2–4). Autoimmune IgGs from preeclampsia patient plasma purified and injected to mice elevate blood pressure and produce oxidative stress and renal pathogenesis in mice akin to human disease (3, 4, 16). In previous studies, we found that the solvent accessibility of –CAFHYESQNST– region of ECL2 is highly sensitive to different states of the AT1R and also to long-range effects of critical receptor mutations in the orthosteric pocket (17, 18). These findings suggested to us that dynamics of the autoantibody epitope might be influenced long range by orthosteric ligands. Hence, we envisage allosteric binding of autoantibody to enhance the efficacy of

Significance

High-resolution structural knowledge is a key driver for discovering small molecules to target functional motifs in G protein-coupled receptors (GPCRs). Reports of autoantibodies targeting extracellular motifs of GPCRs are increasing with no therapies in sight. We address this void using the autoantibody epitope of AT1R as target to discover small molecule inhibitors of AT1R antibody. Resulting inhibitors also exerted allosteric effects on AT1R agonist signaling. This knowledge is useful for consideration of small molecule autoantibody inhibitor development for other GPCRs in which cryptic allosteric sites can be harnessed, and pharmacological intervention with allosteric ligands is desirable. In the case of AT1R, developing new generation of neutral, negative, or positive allosteric ligand therapeutics appears feasible through rational drug design approaches.

Author contributions: K.D.S., Z.P.J., and S.S.K. designed research; K.D.S., Z.P.J., T.H., P.P.S., T.R.P., and R.D. performed research; K.D.S., Z.P.J., T.H., R.D., and S.S.K. contributed new reagents/analytic tools; K.D.S., Z.P.J., T.H., P.P.S., T.R.P., and S.S.K. analyzed data; Z.P.J. provided the iACUC protocol writing and critiqued the manuscript; K.D.S., T.H., and T.R.P. created the figures; S.S.K. provided funding and handled regulatory requirements; and K.D.S. and S.S.K. wrote the paper.

The authors declare no competing interest.

This article is a PNAS Direct Submission.

[1]To whom correspondence may be addressed. Email: karniks@ccf.org.

This article contains supporting information online at https://www.pnas.org/lookup/suppl/doi:10.1073/pnas.2019126118/-/DCSupplemental.

Published August 11, 2021.

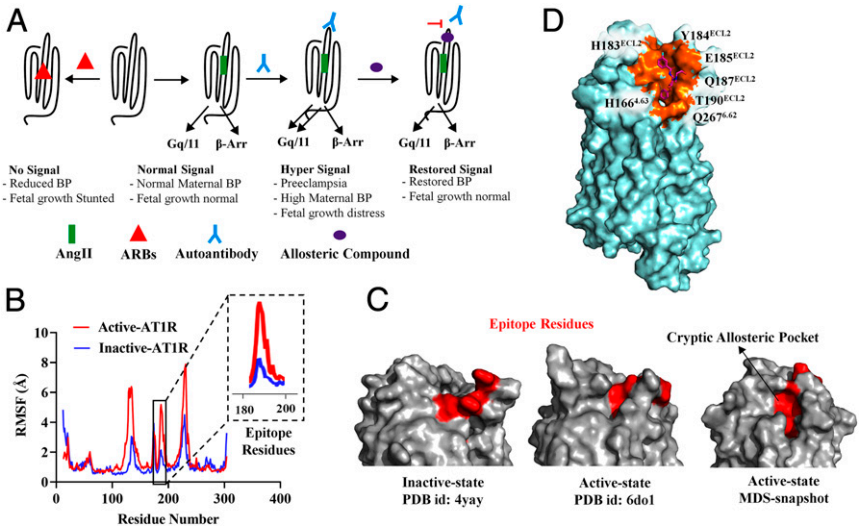

Fig. 1. Autoantibody–dependent pathogenesis and structure-based discovery of the AT1R allosteric pocket including the autoantibody epitope. (*A*) AngII-bound AT1R signals maintain normal blood pressure and fetal growth. Autoantibody binding to the ECL2 epitope enhances AngII signaling producing preeclampsia, maternal hypertension, and fetal growth retardation. ARB binding reverses maternal hypertension. However, ARBs cross the placental barrier, reducing fetal circulation and causing fetopathy. Allosteric ligands designed to inhibit autoantibody binding could restore fetoplacental circulation. (*B*) RMSF of active and inactive state structures of AT1R. (*Inset*) Significant fluctuations of residues in the epitope region, which is indicative of their role in cryptic allosteric pocket formation (*SI Appendix*, Fig. S2). (*C*) Surface view of autoantibody epitope in the extracellular region of inactive and active states of AT1R. A cryptic allosteric pocket is formed during the course of MD simulation. (*D*) A typical docked DCP1 compound is shown with constituent residues of the allosteric pocket highlighted.

orthosteric peptide agonist AngII and partial agonists AngIV and the nonpeptide L-162,313. We propose that autoantibody binding increases G protein and ROS signaling. Hence, the premise for our study is that strategically developing ligands that prevent antibody binding to AT1R could be a treatment paradigm for autoimmune preeclampsia and related disorders (Fig. 1*A*).

Established crystal structures of various states of AT1R facilitated our computation-based approach to unmask a cryptic allosteric pocket that includes the autoantibody epitope and then perform high-throughput virtual screening (HTVS) of small molecule binders to the allosteric pocket. This endeavor yielded compounds with three distinct chemical scaffold structures. In this study, the ability of these compounds to confer selectivity and negative allosteric modulator (NAM) activity in cells and native arterial tissues was investigated. Finally, the efficacy of allosteric compounds to inhibit IgG binding to the autoantibody epitope as well as inhibit IgG-dependent cell signaling was examined. The results validated emergent inhibitors of a GPCR-directed antibody with both in vitro and in vivo NAM activity, thus providing a path to drugging GPCRs.

Results

A Cryptic Allosteric Site in AT1R. Whether the AT1R autoantibody epitope is part of a defined pocket which is druggable was not known. Solvent accessibility and conformational instability of this epitope was shown in earlier studies (10, 11, 13, 15, 17, 18). Further support for the flexibility of this region came from the missing electron densities for epitope residues 187 to 189 in the ∼2.8 Å crystal structures of AT1R inactive states solved with two different antagonists (Protein Data Bank [PDB] identification [ID]: 4yay and 4zud) (10, 13). Flexibility in the epitope region may be essential for the binding antibody and inducing hyperactivation of AT1R. Using Prime Suite (Schrödinger, Inc.), we filled in missing residues in the crystal structure (PDB ID: 4yay) and performed three molecular dynamics (MD) simulations for each ligand-bound complex for 1 μs for each of the three independent simulations as reported previously (15). Ensemble conformations of inactive- (ZD7155 bound; PDB ID: 4yay), apoprotein empty- (ZD7155 unbound; PDB ID: 4yay), and active-state (sAngII bound; PDB ID: 6do1) models of AT1R showed significant conformational differences in ECL2 (*SI Appendix*, Fig. S1*B*). Subsequently, active-state AT1R crystal structures (PDB ID: 6os0, 6os2) solved also showed structural changes in the autoantibody-binding site and in the binding region for G protein and β-arrestin (12, 14). In MD simulation analysis, we observed variability in the average structure of the epitope region in ECL2 in active and inactive states as seen in Fig. 1*B*. The root-mean-square fluctuation (RMSF) plots with SEM error bars for three replicate simulations are shown in *SI Appendix*, Fig. S2. The enlarged plot for the epitope residues elucidates significant change in the conformation of the epitope region between inactive and active states. During the course of MD simulation, the changing shapes of the epitope is observed, which could be the basis for the formation of a cryptic allosteric pocket (*SI Appendix*, Fig. S2). Our MD simulation analysis of the sAngII-bound AT1R structure further validated the cryptic nature of the allosteric pocket (Fig. 1*C*). Significant movement of the epitope region encompassing the allosteric pocket is observed, which further confirms the cryptic nature of the allosteric pocket (Movie S1 and Datasets S1 and S2).

Structure-Based HTVS. To validate its existence and map the shape by identifying small molecules that are able to anchor to the cryptic allosteric pocket, we docked ∼6.8 million compounds from different libraries (Asinex, Maybridge, Chembridge, Zinc). Interactions with AT1R of each molecule in multiple orientations and conformations were scored for van der Waals and electrostatic complementarity that is corrected for context-dependent ligand desolvation. Hits interacting with the orthosteric ligand-binding residues (*SI Appendix*, Fig. S1*A*) Trp84$^{2.60}$, Arg167^{ECL2}, Lys199$^{5.42}$, Asp263$^{6.58}$, and Asp281$^{7.32}$ (superscript indicates the Ballesteros–Weinstein nomenclature of the residue position in AT1R) were eliminated, which yielded hit compounds that bound at topologically distinct pockets of AT1R as shown in *SI Appendix*, Fig. S1*C*. We ranked ∼400 compounds as dense binders to the cryptic allosteric site of AT1R and performed extensive redocking, which yielded 197 hits capable of stable binding to the allosteric pocket.

To ensure the novelty and diversity of final compounds, we performed cluster analysis based on their structural similarity using the Canvas Similarity and Clustering module of Schrödinger. The 197 compounds were grouped into seven clusters (*SI Appendix*, Fig. S3). A representative compound with the best docking score was selected from each cluster. A structural similarity search performed using SciFinder (https://scifinder-n.cas.org) yielded 11 more compounds.

These 18 docking hits were named as DCP1-1 through DCP1-18 in order of their discovery. Chemically, seven belonged to cyclopentane derivatives, two to pyrrolidine derivatives, and six to piperidine derivatives. DCP1-1, -2, and -5 did not belong to the above groups and have different structures (*SI Appendix*, Fig. S4). Next, we performed Glide Induced Fit Docking (IFD) in which the receptor side chains are flexible to give an accurate binding pose (*SI Appendix*, Fig. S5 and Table S1). The 18 compounds showed a docking score of less than −7 with overlapping poses and making unique combinations of interactions (*SI Appendix*, Fig. S1*D*). The residues involved in binding various DCP1 hit compounds provide a more tangible view of the allosteric pocket shape (Fig. 1*D*). These consist of autoantibody epitope residues in ECL2 and transmembrane residues from TM4 and TM6. A total of 13 compounds interact with $His166^{TM4}$, 16 with $His183^{ECL2}$, and 12 with $T190^{ECL2}$. The 18 DCP1 compounds were acquired (from Asinex and Aurora Fine Chemicals LLC) for experimental validation studies. Mass spectrometry and NMR analysis data verified >95% purity of purchased DCP1 compounds, and a subsequent analysis was carried out with stocked compounds.

AT2R has a different ECL2 sequence (*SI Appendix*, Fig. S6*A*), and in ^{125}I-AngIV binding experiments, DCP1 hits did not affect binding to AT2R, demonstrating their receptor subtype specificity (*SI Appendix*, Fig. S6*B*). Since AT2R is a close homolog of AT1R, we examined the possibility of cryptic allosteric pocket formation in the region analogous epitope of AT1R. Three independent MD simulation results did not expose formation of a cryptic allosteric pocket nor significant movement of the region in AT2R (*SI Appendix*, Fig. S6*D*). The Computer Atlas of Surface Topography of Proteins (CASTp) program (19) was used to detect allosteric pockets in related GPCR structures. A docking analysis of DCP1 hits to CASTp-predicted allosteric pockets in AT2R, CCR6, and APJ showed a lower score and MM/GBSA binding energy (*SI Appendix*, Fig. S6 *C*, *E*, and *F* and Table S2). This observation suggests that the allosteric pocket of AT1R is unique. The crystal structure of the allosteric ligand-bound M2 muscarinic receptor is solved. To assess whether the position of the predicted allosteric site of AT1R overlapped with the established position of the allosteric pocket in the ECL2 region of the M2 receptor, we aligned the two GPCRs structurally. The allosteric pocket position in these two GPCRs was distinct, while their orthosteric pockets overlap partly (*SI Appendix*, Fig. S7 *A*–*C*).

Functional Characterization of DCP1 Compounds. A rabbit polyclonal antibody (IgG) for ECL2 sequence –CIENTNITVsAFHYESQNS– was developed as a surrogate for the AT1R autoantibody. The affinity-purified IgG bound specifically to cells permanently expressing AT1R (human embryonic kidney [HEK]-AT1R) and not to HEK293 cells (*SI Appendix*, Fig. S8*A*). Concentration-dependent IgG binding was inhibited by the epitope peptide. The inhibitory potential of the epitope peptide was reduced when we introduced a mutation in the epitope sequence. IgG binding was not inhibited by orthosteric ligands AngII and olmesartan (*SI Appendix*, Fig. S8 *B* and *C*). A similar anti-AT1R antibody which potentiated AngII signaling was previously reported (20). When we screened using a 50-μM concentration to ensure full occupancy, all 18 DCP1 compounds inhibited IgG binding to HEK-AT1R cells (Fig. 2*A*). The inhibition by several DCP1 compounds was significantly greater ($P < 0.001$) relative to the ECL2 peptide, although their inhibitory mechanisms are distinct. The use of the ECL2 peptide is standard practice in AT1R autoantibody–mediated preeclampsia studies (21, 22), which suggests that DCP1 compounds could be promising inhibitors of autoantibody binding to AT1R.

A hallmark of allosteric ligands of GPCRs is their ability to influence orthosteric ligand binding and signaling. We assessed the effect of DCP1 compounds on ^{125}I-AngII binding in HEK-AT1R membranes. All 18 DCP1 compounds did not affect binding, while the orthosteric antagonist olmesartan inhibited ^{125}I-AngII binding (*SI Appendix*, Fig. S9*A*). Increasing concentrations of all 18 DCP1 compounds did not have any appreciable effect on basal calcium signaling in HEK-AT1R cells (*SI Appendix*, Fig. S9*B*). The modulatory effect of DCP1 compounds manifested only in the presence of an orthosteric agonist. The ΔEC_{50} of agonist dose–response curves in the presence of a 30-μM concentration of 18 DCP1 compounds (Fig. 2*B* and *SI Appendix*, Fig. S10 *A*–*L*) indicated their ability to induce a right shift of an agonist dose–response curve, which defines these DCP1 compounds as NAMs.

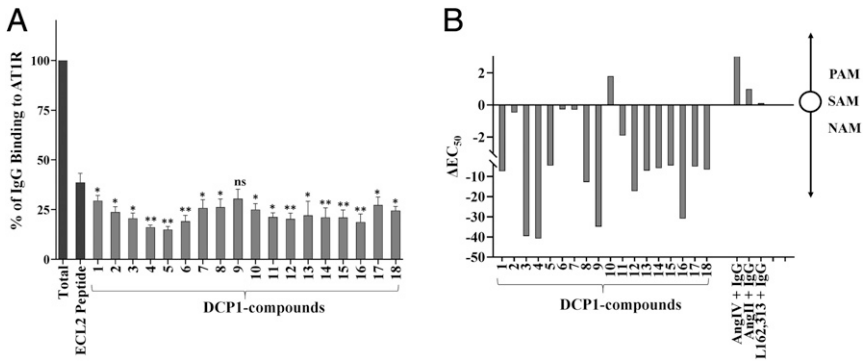

Fig. 2. Comparative effect of DCP1 hit compounds on IgG binding to cell surface AT1R and EC_{50} of AngIV-induced calcium response. (*A*) Binding of IgG to HEK-AT1R cells with and without addition of allosteric ligands. IgG binding inhibition by most DCP1 hit compounds was significant compared to the antigenic peptide used for comparison. The ECL2 peptide was shown to inhibit IgG binding to AT1R in FACS and ELISA experiments (*SI Appendix*, Fig. S8). Although the mechanisms of IgG inhibition by ECL2 peptide and DCP1 hits are expected to be different, benchmarking to epitope–peptide inhibition is a standard practice in preeclampsia research. Hence, the ECL2 peptide inhibition was used as a positive control to compare the inhibitory potential of DCP1 compounds. Inhibition was calculated using (Prism) unpaired Student's *t* test with Welch's correction and yielded statistically significant values, $*P < 0.05$; $**P < 0.001$, and ns implying inconsistent effect. (*B*) Change of EC_{50} for AngIV-induced Ca^{2+} response in the presence of 30 μM indicated allosteric ligands ($n = 3$). EC_{50} shifts (*SI Appendix*, Fig. S10) are calculated using the formula $\Delta EC_{50} = EC_{50}$ AngIV $- EC_{50}$ (AngIV + Allosteric ligands). SAM caused no change in efficacy of agonist, NAM caused negative change in efficacy of agonist, and PAM caused positive change in efficacy of agonist.

Interestingly, the IgG potentiated the calcium response induced by AT1R agonists (Fig. 2*B*). The effective concentration $(EC)_{50}$ change impacted by the IgG was larger for the partial agonist AngIV than full-agonist AngII, an observation that led us to use AngIV as a sensitive probe in our studies. ΔEC_{50} for the non-peptide agonist L-162,313 was modest, and hence, it was not analyzed further. These data indicate that IgG binding to the autoantibody epitope exerts a positive modulatory (PAM) effect, and the magnitude of the PAM effect observed is probe dependent.

Based on the dual properties, the inhibition of IgG binding and NAM potency, we selected DCP1-3 and DCP1-16 (DCP1-4 and DCP1-9 were excluded due to limited availability) for detailed characterization in subsequent experiments.

Effects of DCP1-3 and DCP1-16 Binding on Agonist-Bound AT1R. To gain insight into induced conformational changes when DCP1-3 and DCP1-16 bind to agonist-bound AT1R, we compared DCP1-3+sAngII+AT1R and DCP1-16+sAngII+AT1R complexes to sAngII+AT1R at the end of three independent 1-μs MD simulations. The overall structures of three complexes were similar. Structural differences observed in the ECL2 and orthosteric pocket are shown in Fig. 3 *A*–*C*.

In the orthosteric pocket, the interactions of sAngII with the receptor decreased as observed from MM/GBSA free energy decrease upon binding DCP1-3 for DCP1-16 (*SI Appendix*, Tables S1 and S3). The overall percentage of interactions of the residues, $His256^{6.51}$, $Thr260^{6.55}$, $Asp263^{6.58}$, and $Asp281^{7.32}$, was reduced (Fig. 3 *B* and *C*). These residues are critical for binding and agonist-induced activation of AT1R (12). Surprisingly, the saturation binding of ^{125}I-AngII was unaffected by DCP1 compounds. The binding of the partial agonist ^{125}I-AngIV reduced significantly by DCP1-3 (**$P < 0.001$) and DCP1-16 (*$P < 0.05$) (*SI Appendix*, Fig. S9 *C* and *D*). However, in a competition binding assay, the equilibration of the orthosteric antagonist tracer ^{3}[H]-Candesartan by cold AngII showed a significant increase of the inihibitory concentration $(IC)_{50}$ values in the presence of DCP1-3 ($P = 0.046$) and 16 ($P = 0.042$) (*SI Appendix*, Fig. S9*E*). Changes were observed in ^{3}H-Candesartan B_{max} in the presence of DCP1-3/16; however, the average B_{max} calculated from three independent experiments was not statistically significant. The likely explanation for the lack of DCP1 compound effects on the saturation binding of ^{125}I-AngII is observed in the MD simulation data (Fig. 3*C*). The reduced interaction of AngII with the orthosteric pocket residues was associated with a gain of interaction of Arg^2 in AngII with $Asp16^{Nterm}$ and $Asp17^{Nterm}$ of AT1R in the presence of DCP1-3 and DCP1-16. However, AngIV is a smaller peptide that lacks Arg^2 as shown in *SI Appendix*, Fig. S1*E*. Hence, AngIV cannot interact with $Asp16^{Nterm}$ and $Asp17^{Nterm}$ of AT1R in the presence of DCP1-3 and DCP1-16, which explains the reduction of ^{125}I-AngIV binding. It is known that allosteric NAMs can affect signaling without reducing the binding of orthosteric ligands because often these effects are independent (23). Indeed, a significant decrease of AngII signaling efficacy may be observed due to DCP1 compounds affecting the equilibrium binding of AngII to the AT1R.

ECL2 conformation becomes more stable in the allosteric ligand-bound state, suggesting that the reduced entropic state of ECL2 could prevent the antibody binding observed in Fig. 2*A*. Insight for the stabilization of ECL2 is provided by the binding modes of DCP1-3 and DCP1-16 in AngII-engaged AT1R (Fig. 3*A* and *SI Appendix*, Table S1 and Fig. S5), showing predominant interactions with residues within the autoantibody epitope (e.g., $His183^{ECL2}$, $Tyr184^{ECL2}$) as well as with neighboring portion (e.g., $Glu185^{ECL2}$, $Gln187^{ECL2}$, $Thr190^{ECL2}$). Also, they interact with residues of TM helices (e.g., $Pro162^{4.59}$, $His166^{4.63}$), which contribute further to stabilize ECL2. Both DCP1-3 and DCP1-16 are able to interact with ECL2 and TM helices because they have the same functional groups at position two and three of a cyclopentane scaffold (*SI Appendix*, Fig. S4*A*). The oxygen in the tetrahydropyran ring of DCP1-3 interacts with $Tyr184^{ECL2}$. The methoxy oxygen of DCP1-16 interacts with $Gln267^{6.67}$. Each of these is a unique interaction

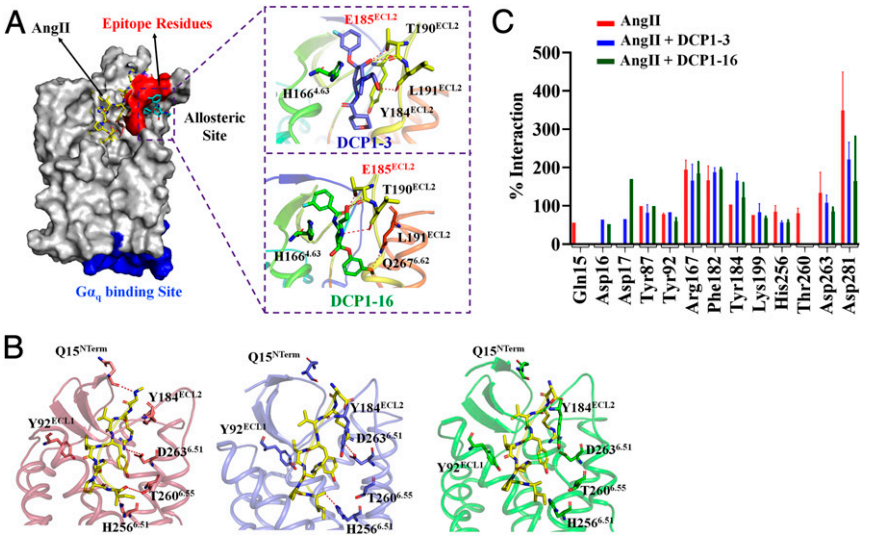

Fig. 3. Interaction of DCP1-3 and DCP1-16 with allosteric pocket and effects on orthosteric ligand interaction. (*A*) AngII-bound AT1R with DCP1-3 bound to the allosteric pocket. IgG epitope is highlighted. An enlargement of the allosteric pocket show poses of DCP1-3 and DCP1-16 (*SI Appendix*, Fig. S5 and Table S1). Sidechains of interacting residues change orientation to accommodate each compound structure. Residues within the epitope for IgG are shown in red. The residue interaction unique to each DCP1 compound is shown in same color as the compound. (*B*) Interactions of AT1R residues with orthosteric peptide ligand sAngII (*Left*) in the presence of DCP1-3 (*Middle*) and DCP1-16 (*Right*). The allosteric pocket–bound DCP1-3 and DCP1-16 are not visible in the MD simulation frames shown. Note the changes in the distance of interaction of each orthosteric pocket sidechain with sAngII in presence of DCP1-3 and DCP1-16. MD simulation predicted similar changes in the interaction of AngII, which may be the basis of its reduced efficacy. The changes in interaction are more exaggerated for AngIV because it is smaller, lacking two N-terminal residues, Asp^1 and Arg^2 (*SI Appendix*, Fig. S1*E*), which cause a reduction of both affinity and efficacy (*SI Appendix*, Fig. S9–S11). (*C*) Change of percent interaction of critical orthosteric pocket residues induced by DCP1-3 (blue) and DCP1-16 (green) compared to percent interaction in their absence (red). Data shown are average of three MD simulations (*SI Appendix*, Tables S1 and S3).

that suggests potential pharmacological differences between DCP1-16 and DCP1-3 (shown in *SI Appendix*, Fig. S5).

To confirm that DCP1-3 and DCP1-16 binding involves interactions with allosteric site residues, we mutated His166$^{4.63}$ in TM helix 4, His183^{ECL2} within the antibody epitope, and Gln187^{ECL2} outside the epitope and tested the mutational effect on ^{125}I-AngIV binding (*SI Appendix*, Fig. S11 *A–D*). Ala replacement in each mutant attenuated the NAM effects of DCP1-3 and DCP1-16 on ^{125}I-AngIV binding, while a significant reduction of binding was evident in the wild type as also seen in *SI Appendix*, Fig. S9*C*. The mutation results confirmed that NAM effects of DCP1-3 and DCP1-16 on ^{125}I-AngIV binding in the wild type requires the residues predicted to be in the allosteric site.

Allosteric Compound Effects on Cell Signaling. To assess the allosteric effects of DCP1-3 and DCP1-16 on AT1R signaling, we evaluated agonist-dependent G protein signaling by intracellular Ca^{2+} release and global cellular changes by dynamic mass redistribution (DMR) measurement (Fig. 4) followed by validation in the mouse aortic vascular smooth muscle cell line, MOVAS-AT1R (see *Methods*).

The Ca^{2+} response curves for the partial agonist AngIV right shifted at indicated concentrations of DCP1-3 and DCP1-16. The EC_{50} shift values are shown in *SI Appendix*, Fig. S12. Inhibition curves estimating the IC_{50} values of DCP1-3 (0.29 μM) and DCP1-16 (3.5 μM) at an EC_{50} dose of AngIV (Fig. 4*A*) recapitulated the negative cooperativity responsible for the NAM effect on this G protein–mediated signal.

DCP1-3 and DCP1-16 had no appreciable effect on AngII-induced calcium response in HEK-AT1R, consistent with the binding experiment (*SI Appendix*, Fig. S9*D*). This may either be due to a silent allosteric modulator (SAM) effect or the masking of a NAM effect due to a high amplification of the signal in HEK-AT1R. We tested this idea in MOVAS-AT1R in which the downstream signal amplification is lesser. DCP1-3 right shifted EC_{50} for the AngII-simulated calcium response 2.5-fold and DCP1-16 by 2.8-fold. Both ligands reduced the E_{max} (*SI Appendix*, Fig. S13*A*). The lack of NAM effect in HEK-AT1R may be due to the masking of the NAM effect due to an amplified AngII signal as opposed to a weak signal by the partial agonist AngIV.

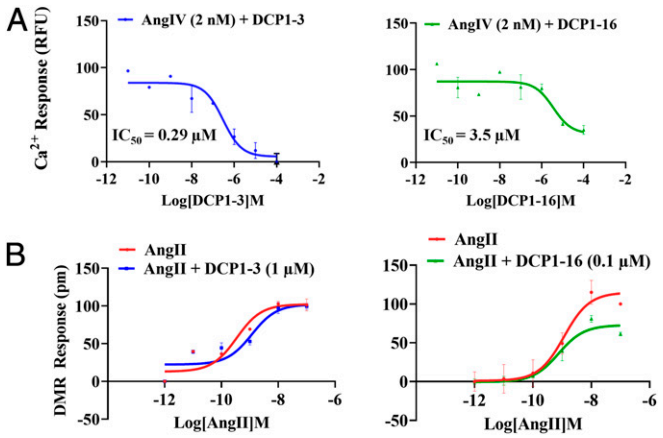

Fig. 4. Modulation of orthosteric agonist efficacy. (*A*) NAM potency of DCP1-3 and DCP1-16 on AngIV at EC_{50} concentration (*SI Appendix*, Fig. S12). Data are mean ± SD calculated from three independent experiments for each run-in triplicate (using Prism). (*B*) NAM effect of DCP1-3 and DCP1-16 on AngII-induced DMR dose response in HEK-AT1R (*SI Appendix*, Fig. S13*B* for MOVAS-AT1R, *SI Appendix*, Fig. S14). A representative experiment run-in triplicate is shown. Mean ± SD calculated in three independent measurements indicates that the EC_{50} shift is statistically significant ($P < 0.05$).

DMR is a sensitive measure of global cellular changes brought about by receptor signaling without the use of chemical dyes or labels to monitor cellular events. DMR signal changes were AngII dose dependent, and the signal was completely inhibited by ARB treatment (*SI Appendix*, Fig. S14*A*). In the presence of DCP1-3 and DCP1-16, the DMR indicated a decrease in the functional response (Fig. 4*B*). The IC_{50} values estimated at 0.1 μM AngII concentration was 10 μM for DCP1-3 and 6.5 μM for DCP1-16 (*SI Appendix*, Fig. S14 *B–C*), demonstrating the NAM effect on AngII-mediated cellular signaling by the AT1R. A similar effect was observed for the DMR signal in MOVAS-AT1R cells (*SI Appendix*, Fig. S13*B*).

The induction of signal bias by allosteric ligands is an emerging concept of significant interest and an important step in the allosteric drug discovery process (24, 25). Therefore, the effects of DCP1-3 and DCP1-16 on β-arrestin recruitment by the receptor were examined by the Tango assay (26) and confocal microscopy on HEK-AT1R cells expressing β-arrestin1–EGFP. No significant changes in AngII-mediated β-arrestin recruitment were observed in the presence of DCP1-3/16.

AngIV produced a weak and inconsistent signal in DMR, PRESTO-Tango, and myograph assays. Being unable to detect reproducible AngIV response in these assays, presumably due to its weak partial agonist character, we did not examine DCP1 compound effects on AngIV any further.

Effect of DCP1-3 and DCP1-16 on AngII-Induced Artery Contraction. Following the confirmation of an allosteric effect of DCP1-3 and DCP1-16 on AngII signaling in cells, we tested their ability to modulate AT1R in functional assays. To characterize the NAM effect on a physiological system, we employed an ex vivo model, the constriction of live renal and iliac artery segment explants from mice in a myograph chamber (*SI Appendix*, Fig. S15*A*). The preservation of endothelium and vessel integrity was confirmed by measuring contraction/relaxation responses to high potassium physiological salt solution (KPSS), phenylephrine, and acetylcholine. Vasoconstriction is a well-established physiological response to AngII activation of the AT1R that is inhibited by ARBs such as olmesartan (27, 28). In our experimental system, an AngII-induced contractile response was inhibited by olmesartan (*SI Appendix*, Fig. S15*B*) but not by the AT2R inhibitor PD123319. DCP1 compounds on their own exerted no detectable effect on the vessels. There was no contraction and relaxation signal nor a loss of responsiveness in renal and iliac arteries when only DCP1-3 or DCP1-16 was infused into the myograph chamber, which is an indication of the safety of these compounds.

We then determined the magnitude of the contraction induced by AngII in the absence or presence of DCP1-3 and DCP1-16. Explants obtained from male and female mice were exposed to 200 nM AngII or 200 nM AngII+DCP1-3 (30 μM) and 200 nM AngII+DCP1-16 (30 μM) and vasoconstriction was monitored (*SI Appendix*, Fig. S15*C*). In both renal and iliac arteries, DCP1-3 and DCP1-16 reduced AngII-induced contraction (Fig. 5 *A* and *B*). The AngII-induced constriction of renal and iliac arteries was significantly reduced ($P < 0.05$) in both male and female mice when treated with DCP1-3 and DCP1-16 (Fig. 5*C*). The inhibitory effect was reversed by washing the vessels treated with DCP1 compounds and restimulating with AngII, which reproduced the magnitude of contraction by AngII prior to treatment (*SI Appendix*, Fig. S15*C*). The ex vivo experiments showed the preservation of NAM properties of DCP1-3 and DCP1-16 in live arteries in both genders.

Our results reflect the well-established gender effect on AngII signaling (29) influencing the efficacy of DCP1 compound potency for vasoconstriction response in females. It is unlikely that the gender effect changes DCP1 compound's autoantibody blocking efficacy. Therefore, it appears that suitable allosteric drug candidates can be developed for autoantibody inhibition in preeclampsia

PHARMACOLOGY

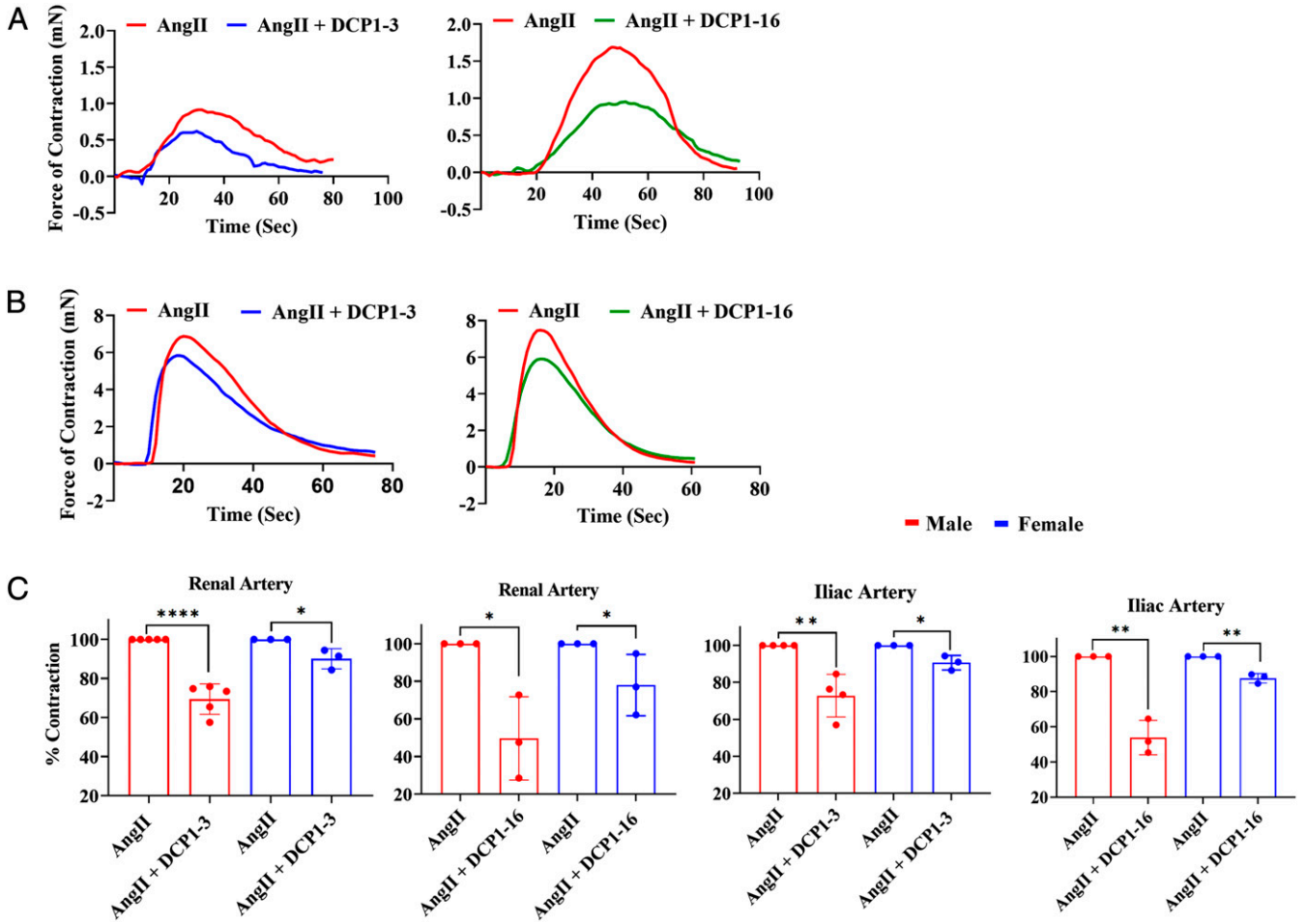

Fig. 5. Effects of DCP1-3 and DCP1-16 on AngII-induced vessel contraction. (*A* and *B*) Contraction of renal (*A*) and iliac (*B*) arteries induced by AngII in the absence (red) and presence of DCP1-3 (blue) and DCP1-16 (green). Approximately 100,000 data points per millisecond recorded in each response trace was averaged per seconds for plotting the response curves shown using our in-house Python script for myograph.py after baseline corrections. To ensure intact endothelium and vessel behavior, responses to KPSS, phenylephrine, and acetylcholine were initially assessed (*SI Appendix*, Fig. S15). (*C*) Effects of 30 μM DCP1-3 and DCP1-16 on 200 nM AngII-induced vasoconstriction ex vivo. Each bar represents the average ± SD of response readings in the number of mice indicated in filled circles on each bar. Male and female mice were used because the vascular response to AngII is influenced by gender. The results reflect well-established gender bias (dimorphism) in AngII signaling through AT1R. Reduced NAM effects of DCP1 compounds in females may be relevant to future allosteric drug development strategies. ****$P < 0.001$, **$P < 0.05$, *$P = 0.05$.

with a lower risk of causing undesirable hypotension, leading to reduced fetoplacental circulation and fetopathy in females.

Inhibition of Antibody-Enhanced Signaling by DCP1-3 and DCP1-16. The efficacy of inhibition of IgG binding to HEK-AT1R cells was assessed. The IC_{50} values of DCP1-3 and DCP1-16 were 2.9 and 0.6 nM, respectively (Fig. 6*A*). The inhibition of IgG binding by DCP1-3 and DCP1-16 resulted in reversing the PAM effect of the IgG on the agonist-induced calcium response (Fig. 6*C*).

To establish "probe dependence" of the PAM effect of the IgG as observed for most GPCR allosteric modulators (30, 31), we determined the effects of IgG on dose–response curves of different orthosteric agonists, AngIV, AngII, and L-162,313. IgG produced the PAM effect on all three agonists, demonstrating functional cooperativity for the three orthosteric agonists (Fig. 6*B*).

Finally, we confirmed the PAM effect of IgG in the ROS production assay in both HEK-AT1R and MOVAS-AT1R cells. The PAM effect of IgG was reversed significantly by both DCP1-3 and DCP1-16 (Fig. 6*C* and *SI Appendix*, Fig. S13*C*). These data reveal that DCP1-3 and DCP1-16 effectively block IgG binding to AT1R in cells as well as the agonist potentiating PAM effects of the IgG on cellular signaling, which indicate that small molecule inhibitors of IgG binding to AT1R could have clinical significance.

Discussion

This study highlights three inferences pertinent to the biology of AT1R. First, at the beginning of this study, the existence of a druggable allosteric site in AT1R was far from certain to us, although allosteric sites have been found in the extracellular region of other GPCRs (24, 30, 31). We envisaged a sterically undefined allosteric site on AT1R primarily based on preeclampsia autoantibody literature (2–8) combined with our previous experiments which showed that solvent accessibility of epitope residues changes in response to orthosteric ligand binding (10, 11, 13, 15, 17, 18). MD simulation based on crystallographic structures of AT1R also supported the prospect of a cryptic pocket (Fig. 1*C*). The existence of this pocket is experimentally supported here by a characterization of the PAM effect caused by epitope-specific IgG binding (Figs. 2*B* and 6) and NAM effects of DCP1 compound binding to epitope residues within the allosteric pocket (Fig. 1*D* and *SI Appendix*, Fig. S11). The allosteric site includes the preeclampsia epitope, and as shown here, IgG binding is inhibited by the DCP1 compounds (Figs. 2*A* and 6 and *SI Appendix*, Figs. S8 and S13*C*).

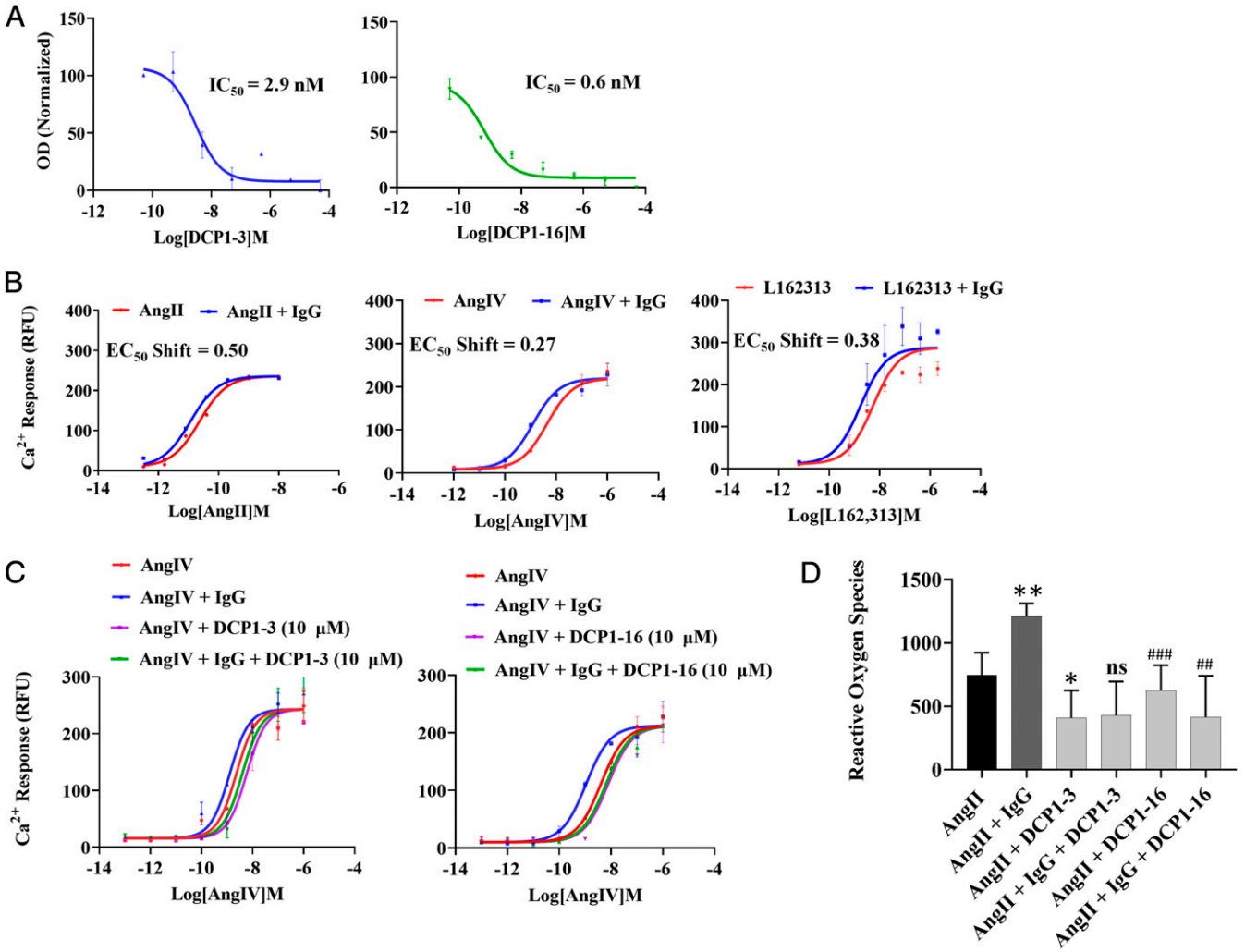

Fig. 6. Effects of DCP1-3 and DCP1-16 on AngII signaling in HEK-AT1R cells in the presence of IgG. (*A*) Inhibition potency of DCP1-3 and DCP1-16 on IgG binding, presumably by the sequestration of residues which are solvent accessible in absence of DCP1 compounds. (*B*) Positive modulation of potency of three AT1R agonists by IgG from a representative experiment for each performed in triplicate is shown. The values are an average of three experiments. (*C*) Reversal of IgG-induced agonist potency shift by DCP1-3 and DCP1-16. A representative experiment for each treatment performed in triplicate is shown. (*D*) IgG potentiated AngII-induced ROS production is inhibited by DCP1-3 and DCP1-16. $^{*}P < 0.05$ change compared to AngII and $^{\#\#}P < 0.05$ and $^{\#\#\#}P < 0.001$ change compared to IgG + AngII and ns, not significant. Also see effects of DCP1-3 and DCP1-16 on AngII signaling in MOVAS-AT1R cells (*SI Appendix*, Fig. S13*C*). Three independent experiments were performed, each in triplicate. Data presented here is representative of one experiment and is statistically significant ($^{**}P < 0.05$ changes compare to AngII and AngII + IgG).

Since DCP1 compound binding increased ECL2 stability in MD simulation, we presume that the epitope residues become inaccessible for IgG binding when the site is occupied by the allosteric ligand. The confirmation of this mechanism and allosteric ligand-binding interactions with atomic resolution accuracy remains to be fully documented. Our finding is an advancement which could stimulate future development of more potent small molecule inhibitors of AT1R autoantibodies for managing disease states such as preeclampsia.

Secondly, small molecule targeting of the allosteric site of AT1R revealed in our study opens the opportunity for moderating receptor subtype–specific AngII signaling efficacy, which was not possible till now. Structure-guided small molecule library screening targeting the allosteric site resulted in 18 compounds. Nine out of 18 molecules obtained from screening were cyclopentane and pyrrolidine derivatives, and six out of 18 molecules were piperidine derivatives (*SI Appendix*, Fig. S4). These compounds docked well without competing with orthosteric ligands or altering the basal activity of AT1R and acted as NAMs only in the presence of orthosteric agonists of AT1R in cells and arteries (Figs. 2 and 4–6). The NAM potencies of compounds were modest, but this is not surprising, as this discovery effort took advantage of cataloged chemical library compounds. In this study, we did not make attempts to modify and measure the effect of different R-groups and scaffold structures as accomplished in various SAR studies. Nonetheless, most of the allosteric modulatory effects of DCP1-3 and DCP1-16 were similar but not identical. We cannot attribute the differential effects of DCP1-3 and DCP1-16 simply to the difference in positions of R-groups and docking poses (Fig. 3*A* and *SI Appendix*, Figs. S4 and S5), which will require further experiments. The mutagenesis study (*SI Appendix*, Fig. S11) is not sufficient to distinguish among multiple binding poses of DCP1 compounds. A systematic structure–activity relationship analysis of analogs and finally the determination of allosteric ligand-bound crystal structures are required to fully validate the binding poses of DCP1 compounds. We were able to confirm AT1R specificity of our docking hits by molecular docking and an MM/GBSA study of closely related GPCRs including AT2R, CCR6, APJ, and the M2

muscarinic receptor (*SI Appendix*, Table S2 and Figs. S6 and S7). An important feature of these allosteric modulators is their chemical novelty—they do not resemble any known AT1R and AT2R ligands. An analysis of their binding mode confirms exclusion of AT1R orthosteric pocket residues known to be critical for orthosteric ligand binding including the important $Arg167^{ECL2}$ on ECL2 (11, 15), which establishes their novelty.

The allosteric site of AT1R is a viable target for novel drug development. Finding the DCP1-hits is encouraging for utilizing structure-based computational approaches in the discovery of a new generation of AT1R-targeted therapeutics. However, the caveats of small molecule design through MD simulation and in silico docking approaches are that they are unpredictive of SAM, PAM, and NAM properties of those ligands or their therapeutic efficacies. Indeed, the efficacy of compounds we discovered are modest, and we did not attempt to search for a fully optimized allosteric hit or develop a lead compound in this study. However, we imagine DCP1 docking hits to serve as templates for systematic drug development efforts to better inhibit activating autoantibodies as well as in the development of hypertension modulators of improved potency as SAM or NAM for regulating AngII pathophysiology in cardiovascular diseases (32). Another possibility is to search for PAMs of AT1R, which may have an application in the treatment of chronic hypotensive disorders (33, 34).

Finally, the opportunity for developing and preclinical testing of SAM (or weak NAMs) now exists that can function as potent inhibitors of AT1R-targeting autoantibody without undesired side effects. Maternal blood pressure regulation by the hormone AngII sustains fetal growth through fetoplacental circulation. Therefore, inhibitors for preeclampsia management should be devoid of toxic polypharmacological consequences or metabolic transformation causing deleterious fetal effects when they cross the placental barrier. Such allosteric ligands may also have therapeutic potential for treating hypertensive and kidney pathology during pregnancy. Maternal blood pressure regulation by the hormone AngII sustains fetal growth through fetoplacental circulation. Unlike traditional ARBs and ACEi, SAMs of AT1R would not inhibit AngII-dependent fetal physiology and development but inhibit the PAM effects of autoantibodies on maternal physiology (3–6, 9, 16). Developing autoimmune therapy directed to AT1R through designed drugs may be widely beneficial. For instance, AT1R autoantibodies cause a variety of pathologies, including adrenal hyperplasia, hyperaldosteronism, renal graft rejection, and organ transplantation failures (7, 8, 35, 36), for which there are no current treatments. The approach we describe here may serve as a blueprint for searching cryptic allosteric sites in crystal structures and generating inhibitors of autoantibodies targeting other GPCRs. When these goals are achieved, the small molecule inhibitor treatment of autoimmune GPCR disorders may advance toward clinical applications.

Methods

Details regarding experimental conditions and reagents are provided in *SI Appendix, SI Methods*.

Protein Preparation. The starting coordinates of AT1R (PDB IDs: 4yay, 6do1, 6os0, 6os1, 6os2) (10, 12, 14) were retrieved from the PDB (https://www.rcsb.org). The 4yay structure was modified for Glide docking calculations (Glide, Schrödinger, Inc.) (11, 37). The default protocol of OPLS3 (Optimized Potentials for Liquid Simulations, Schrödinger, Inc.) force field energy minimization was applied for the calculations in Protein Preparation Wizard (38). Missing segments of loops were filled in using Prime, Schrödinger, during the protein preparation (39). Details of MD simulation analysis generating the Ensemble conformations of inactive- (ARB bound), apoprotein empty– (ARB unbound) and active-state AngII-bound structures are described in our previous papers (11, 15). In our current MD simulation studies, five average structures for each state were generated and used for structure-based screening of the compound library.

Compound Database. The compounds were collected from Zinc, Asinex, and Maybridge, Chembridge database (~6.7 million compounds). Lipinski-filtered compounds were cleaned using LigPrep (40) with the expansion of stereo centers whose chirality was unspecified. This small molecule collection contains a high percentage of drug-like compounds.

HTVS. Glide-implemented virtual screening workflow was used to rank compounds by HTVS and then by standard precision (SP) and extra precision (XP) docking for higher accuracy. The center of mass position of the ECL2 residues 181, 182, 183, 184, 185, 186, and 187 was set as the grid center for the allosteric site. The inner and outer box values were set to 10 and 25 Å, respectively (37, 41). All the compounds were docked by HTVS, SP, and XP stages of the protocol. The glide score and glide energy, the specific ligand–protein interaction energies, hydrophobic interactions, hydrogen bonds, internal energy, π–π stacking interactions, RMSF, and de-solvation parameters are applied for selecting potential allosteric hits as described in other studies (42–45).

IFD. Schrödinger's IFD module was used to dock hits to our proposed allosteric site. First, using Glide XP mode, the ligand was docked into a rigid receptor model with scaled down vdW radii, and ligand poses were retained for protein structural refinements. A vdW scaling of 0.5 was used for both the protein and ligand nonpolar atoms. A constrained energy minimization was carried out keeping the protein structure close to the original crystal structure while removing bad steric contacts using the OPLS3 force field with an implicit solvation model. Prime, Schrödinger, was then used to generate the induced-fit protein–ligand complexes. In the final step, each ligand was redocked into the top 20 refined structures using Glide XP (46, 47) and Prime/MM-GBSA for all the protein–ligand complexes as reported earlier (11, 15).

MD Simulations. MD simulations were carried out for AT1R-apo (ARB unbound; PDB ID: 4yay) and AT1R-AngII complexes as reported earlier (15) using Desmond MD code and the OPLS3 forcefield (38). We ran three MD simulations for 1 μs for each of the three independent simulations for each of the complexes (AT1R-sAngII, AT1R-sAngII-DCP1-3, and AT1R-sAngII-DCP1-16). Using the Desmond system builder, a 10-Å buffered orthorhombic system with periodic boundary conditions was constructed using a phosphatidylcholine (POPC) lipid membrane and a single point charge (SPC) explicit water solvent as detailed in our papers (11, 15). Before each MD simulation, a default Desmond membrane protein relaxation protocol was applied (48–51).

^{125}I-Ang Peptide-Specific Binding Analysis. Membranes prepared from the HEK293T clone permanently expressing wild-type HA-AT1R were used as described earlier (10, 13, 17, 18). Competition binding assays were performed under equilibrium conditions using radioligands (2 nM ^{125}I-AngII or [^{3}H]-Candesartan and 0.04 and 1,000 nM concentrations of the competing ligand). The binding reaction was terminated by filtering through Brandel GF/C glass fiber filters, and after a wash with buffer, the bound ligand's counts/min was measured (MicroBeta2 Plate Counter, PerkinElmer Life Sciences). A total of 10^{-5} M ^{125}I-AngII (Bachem) was used to measure nonspecific binding. The [^{3}H]-Candesartan tracer competition binding was performed under conditions identical to ^{125}I-AngII competition binding. The filter membranes were soaked in 7 mL Ecoscint A scintillation fluid (National Diagnostics) and incubated for 1 h at room temperature. The bound ligand fraction was determined as the disintegrations/min using a Beckman LS 6000 Liquid Scintillation Counter (Global Medical Instrumentation). The binding kinetics were analyzed by the nonlinear curve-fitting program in GraphPad Prism 8. The means ± SE for the IC_{50} values were calculated from three to five independent experiments as described earlier (10, 13).

Effect on Saturation Binding of Peptide Agonists. Saturation binding assays were performed using a 0.0- to 1.6-nM range of ^{125}I-AngII and a 0.0- to 27-nM concentration range of ^{125}I-AngIV without and with 50 μM DCP1-3 and DCP1-16 compounds. Mean ± SE for the K_d and B_{max} values were analyzed by the nonlinear curve-fitting program GraphPad Prism 8 as reported (10, 13).

ECL2 Antibody Production in Rabbit and Affinity Purification/Characterization of IgG Specificity. The peptide antigen -CIENTNITVsAFHYESQNS- was conjugated to keyhole limpet hemocyanin (KLH). Please note the "s" substitution in the sequence for C, which was made to prevent disulfide bond formation, and N-terminal C was introduced to link the peptide to KLH. Serum was

collected from sham, and peptide-injected rabbits were collected, and the specific antibody titer was measured by enzyme-linked immunosorbent assay (ELISA) using the peptide -CIENTNITVsAFHYESQNS- coated on a 96-well plate. The antigenic peptide -CIENTNITVsAFHYESQNS- was linked to Pierce's Sulfo-Link Immobilization resin (Pierce, catalog no. 44999) for generating the peptide affinity column. The peptide-specific antibody was purified per manufacturer's recommendations.

ELISA. HEK-AT1R cells were grown overnight (600,000 cells/well) in poly-l-lysine–coated 24-well clear bottom plates. Cell were washed with WB1 (1% bovine serum albumin [BSA] in Hanks Balanced Salt Solution [HBSS]) and then fixed with 4% paraformaldehyde (PFA) and washed. Cells were treated with DCP1 compounds for 1 h at room temperature and then incubated with 1:1,000 diluted ECL2 antibody (Aab) for 1 h. Plates were washed and peroxidase conjugated anti-rabbit secondary antibody was added for 1 h and then washed with WB2 (0.5% BSA in HBSS). A total of 200 μL OPD (phosphate-citrate buffer with sodium perborate + *o*-Phenylenediamine dihydrochloride) was added and allowed to develop color for 15 min. The reaction was stopped by adding 3N HCl and absorbance was read at 492 nm on the Flexstation 3, Molecular Devices. The percentage of inhibition data were normalized and analyzed using the sigmoidal dose–response function built into GraphPad Prism 8.0.

Comparative Agonism by Intracellular Calcium Levels. Calcium levels were measured using the Fluorescent Imaging Plate Reader Calcium 5 Assay kit (Molecular Devices) as described previously (10). HEK-AT1R or MOVAS-AT1R cells (100,000 cells/well) were seeded in a 96-well clear bottom black plate. Following serum starvation of cells, calcium-sensitive dye was added. Flexstation3 was programmed to add ligands (0.04 and 1,000 nM concentration) to the cells and monitor the fluorescence before and after the addition of ligands. Changes in intracellular calcium were recorded by measuring ΔF/F (max-min) and are represented as relative fluorescence units. The dose–response curves were calculated assuming 100% stimulation by AngII. Data were analyzed using the sigmoidal dose–response function built into GraphPad Prism 8.0.

Vascular Reactivity. Vascular contraction studies were conducted following the NIH guidelines for care and use of animals (52) and with approved mouse protocols from the Institutional Animal Care and Use Committee. C57BL/6 male and female mice were euthanized, and 1.5- to 2-mm length renal and iliac artery segments were dissected, transferred to a dish containing physiological saline solution, and the perivascular fat tissue was removed. Vessels were then mounted in multiwire myograph system (Danish Myo Technologies) model 620N and incubated at 37 °C under constant rate aeration with 5% CO_2 and 95% O_2. Normal resting tension was determined. The integrity of the vessels was assessed by a) voltage-dependent contraction induced by receptor-independent depolarization of the vascular smooth muscle by elevated KPSS and b) receptor-dependent contraction and relaxation, which were induced by α_1-adrenergic and muscarinic stimulation with phenylephrine and methylcholine, respectively. Vessels that passed the integrity test were used to assess AngII-dependent contraction. Responses were recorded by using computerized data acquisition and recording software LabChart 8 (AD Instruments).

AngII-Dependent Contraction. AngII caused contraction in renal and iliac arteries from male and female mice. AngII-dependent contraction was lower in females than males. To overcome the gender effect, AngII contraction in female arteries was performed in the presence of 100 μmol/L N(gamma)-nitro-L-arginine methyl ester, a nitric oxide synthase inhibitor, as reported earlier (29). To test the efficacy of DCP1 compounds, vessels were contracted with 2 nM AngII and allowed to return to baseline by wash out. The second stimulation was performed with AngII +30 μM DCP1-3 or 30 μM DCP1-16. After the wash out, a third stimulation with AngII alone and fourth with AngII+ARB was performed to ascertain, respectively, the preservation of AngII response and AT1R selectivity through the experiment. Statistical analyses were performed after assessing the normal distributions of data. In Fig. 5*C* asterisks, $*P < 0.05$, $**P < 0.005$, $***P < 0.0005$, and $****P < 0.0001$ indicate significance of difference between AngII and AngII+DCP1 compound treatments (calculated using unpaired Student's *t* test).

DMR Studies on HEK-AT1R Cells. DMR experiments were performed on HEK-AT1R and MOVAS-AT1R cells grown in 96-well DMR microplates as described earlier (53). Cells were washed with 1× HBSS buffer and allowed to adapt to room temperature. Basal- and ligand-dependent DMR responses were monitored in a Corning Epic BT system (Corning Epic product code 5053). A stable baseline signal is set as zero. Thereafter, a change in DMR signal when different concentrations of the ligands of interest are added was recorded. DCP1-3 and DCP1-16 (final concentration 0.1 μM) were incubated with cells prior to AngII stimulation to assess their NAM effect. DMR response graphs (in pm/min) were generated from collected raw data analyzed using Corning Epic Analyzer software.

β-Arrestin Recruitment. Details for the PRESTO-Tango assay (26, 54, 55) and confocal microscopy analysis of β-arrestin1–EGFP recruitment are provided in *SI Appendix, SI Methods*.

ROS. Cells were plated and the next day changed to serum free, clear medium for 2 h. Cells were treated with 100 nM AngII for 4 h, washed, and then incubated in 8 μM of the membrane-permeable ROS-sensitive probe 5-(and-6)-chloromethyl-2′,7′-dichlorodihydrofluorescein diacetate acetyl ester (CM-H2DCFDA) (Molecular Probes) for 45 min. CM-H2DCFDA is converted by intracellular esterases to the membrane-impermeable compound, 2′ 7′–dichlorofluorescein, in the presence of H_2O_2. Fluorescence intensity was measured at 495 nm excitation and 517 nm emission using Flexstation 3. Ter-butyl hydroperoxide was used as a positive control. Data were compared using unpaired Student's *t* test with Welch's correction in GraphPad Prism 8.

AT1R Mutant Characterization. Complementary DNA encoding the wild-type and mutant (166A, 183A, 187A) HA-AT1R cloned into a pcDNA3.1 expression vector (GenScript). HEK293T cells (3×10^6 per 10 cm diameter plate) grown overnight were transiently transfected with wild-type or mutant plasmid DNA using FuGENE 6. Between 60 to 70 h after transfection, cells were harvested, and total membranes were prepared for radio ligand-binding analysis as described (10, 13, 17, 18).

MOVAS Cells Expressing AT1R. SV40 large T antigen immortalized MOVAS acquired from the American Type Culture Collection (ATCC) (catalog no. ATCC CRL-2797). MOVAS did not show a measurable Ca^{2+} response to AngII and hence were transfected with pcDNA-HA-AT1R plasmid bearing the hygromycin resistance gene. The MOVAS-AT1R clone, resistant to 200 μg/mL hygromycin selection, stably expressed HA-AT1R as determined by fluorescence-activated cell sorting (FACS) analysis using the anti-HA Alexa Fluor 488 (Cell Signaling Technology catalog no. 2350S). The chosen MOVAS-AT1R clone bound ^{125}I-AngII (0.9 pmol/mg membrane protein) that is blocked by AT1R antagonist olmesartan but not by the AT2R antagonist PD123319. AngII-induced Ca^{2+} signaling in MOVAS-AT1R was also inhibited by olmesartan but not by PD123319.

Data Availability. Coordinates of MD simulation data have been deposited in the Protein Model Database (PM0084131, PM0084132). All other study data are included in the article and/or supporting information.

ACKNOWLEDGMENTS. We thank the Lerner Research Institute (LRI) FACS and Protein and Peptide Biochemistry Cores and Dr. Stanley Hazen for providing access to the DMR instrument. We thank Abdo Boumitri for the construction of AT1R-Tango plasmid used in our Tango assays. We extend thanks to Earl Poptic and the LRI Hybridoma Core for assistance in the production of rabbit IgG. We thank Michael Weiner of the LRI Computer Support Core facility for Linux support. This work was supported by NIH RO1 Grants HL132351 (S.S.K.) and HL142091 (S.S.K.) and an Innovation Award from LRI.

1. C. Meyer, H. Heidecke, Antibodies against GPCR. *Front. Biosci.* **23**, 2177–2194 (2018).
2. H. Unal, R. Jagannathan, S. S. Karnik, Mechanism of GPCR-directed autoantibodies in diseases. *Adv. Exp. Med. Biol.* **749**, 187–199 (2012).
3. D. Dragun, The role of angiotensin II type 1 receptor-activating antibodies in renal allograft vascular rejection. *Pediatr. Nephrol.* **22**, 911–914 (2007).
4. Y. Xia, R. E. Kellems, Angiotensin receptor agonistic autoantibodies and hypertension: Preeclampsia and beyond. *Circ. Res.* **113**, 78–87 (2013).
5. World Health Organization, Maternal mortality. https://www.who.int/news-room/fact-sheets/detail/maternal-mortality. Accessed 19 September 2019.
6. Centers for Diseases Control and Prevention, High blood pressure during pregnancy. https://www.cdc.gov/bloodpressure/pregnancy.htm. Accessed 6 May 2021.
7. X. Zhang, N. L. Reinsmoen, Impact and production of non-HLA-specific antibodies in solid organ transplantation. *Int. J. Immunogenet.* **47**, 235–242 (2020).
8. T. A. Williams *et al*., Diverse responses of autoantibodies to the angiotensin II type 1 receptor in primary aldosteronism. *Hypertension* **74**, 784–792 (2019).
9. World Health Organization, WHO recommendations for prevention and treatment of pre-eclampsia and eclampsia. https://www.who.int/reproductivehealth/publications/maternal_perinatal_health/9789241548335/en/. Accessed 3 August 2021.

10. H. Zhang *et al*., Structural basis for ligand recognition and functional selectivity at angiotensin receptor. *J. Biol. Chem.* **290**, 29127–29139 (2015).
11. K. D. Singh, H. Unal, R. Desnoyer, S. S. Karnik, Divergent spatiotemporal interaction of angiotensin receptor blocking drugs with angiotensin type 1 receptor. *J. Chem. Inf. Model.* **58**, 182–193 (2018).
12. L. M. Wingler *et al*., Angiotensin and biased analogs induce structurally distinct active conformations within a GPCR. *Science* **367**, 888–892 (2020).
13. H. Zhang *et al*., Structure of the angiotensin receptor revealed by serial femtosecond crystallography. *Cell* **161**, 833–844 (2015).
14. L. M. Wingler, C. McMahon, D. P. Staus, R. J. Lefkowitz, A. C. Kruse, Distinctive activation mechanism for angiotensin receptor revealed by a synthetic nanobody. *Cell* **176**, 479–490.e12 (2019).
15. K. D. Singh, H. Unal, R. Desnoyer, S. S. Karnik, Mechanism of hormone peptide activation of a GPCR: Angiotensin II activated state of AT_1R initiated by van der Waals attraction. *J. Chem. Inf. Model.* **59**, 373–385 (2019).
16. C. C. Zhou *et al*., Angiotensin receptor agonistic autoantibodies induce pre-eclampsia in pregnant mice. *Nat. Med.* **14**, 855–862 (2008).
17. H. Unal, R. Jagannathan, M. B. Bhat, S. S. Karnik, Ligand-specific conformation of extracellular loop-2 in the angiotensin II type 1 receptor. *J. Biol. Chem.* **285**, 16341–16350 (2010).
18. H. Unal *et al*., Long range effect of mutations on specific conformational changes in the extracellular loop 2 of angiotensin II type 1 receptor. *J. Biol. Chem.* **288**, 540–551 (2013).
19. W. Tian, C. Chen, X. Lei, J. Zhao, J. Liang, CASTp 3.0: Computed atlas of surface topography of proteins. *Nucleic Acids Res.* **46**, W363–W367 (2018).
20. K. Wenzel *et al*., Angiotensin II type 1 receptor antibodies and increased angiotensin II sensitivity in pregnant rats. *Hypertension* **58**, 77–84 (2011).
21. S. Zhang *et al*., Angiotensin type 1 receptor autoantibody from preeclamptic patients induces human fetoplacental vasoconstriction. *J. Cell. Physiol.* **228**, 142–148 (2013).
22. H. Li *et al*., Novel retro-inverso peptide inhibitor reverses angiotensin receptor autoantibody-induced hypertension in the rabbit. *Hypertension* **65**, 793–799 (2015).
23. T. Kenakin, R. T. Strachan, PAM-antagonists: A better way to block pathological receptor signaling? *Trends Pharmacol. Sci.* **39**, 748–765 (2018).
24. C. W. Lindsley *et al*., Practical strategies and concepts in GPCR allosteric modulator discovery: Recent advances with metabotropic glutamate receptors. *Chem. Rev.* **116**, 6707–6741 (2016).
25. F. Landomiel *et al*., Biased signaling and allosteric modulation at the FSHR. *Front. Endocrinol. (Lausanne)* **10**, 148 (2019).
26. W. K. Kroeze *et al*., PRESTO-Tango as an open-source resource for interrogation of the druggable human GPCRome. *Nat. Struct. Mol. Biol.* **22**, 362–369 (2015).
27. A. A. Al-Majed, A. H. H. Bakheit, H. A. Abdel Aziz, A. A. M. Al-Jallal, Olmesartan. *Profiles Drug Subst. Excip. Relat. Methodol.* **42**, 241–286 (2017).
28. X. Zhang, H. Zhang, Y. Ma, W. Che, M. R. Hamblin, Management of hypertension using Olmesartan alone or in combination. *Cardiol. Ther.* **6**, 13–32 (2017).
29. H. Ji *et al*., Sex chromosome effects unmasked in angiotensin II-induced hypertension. *Hypertension* **55**, 1275–1282 (2010).
30. S. Maeda, Q. Qu, M. J. Robertson, G. Skiniotis, B. K. Kobilka, Structures of the M1 and M2 muscarinic acetylcholine receptor/G-protein complexes. *Science* **364**, 552–557 (2019).
31. A. C. Kruse *et al*., Activation and allosteric modulation of a muscarinic acetylcholine receptor. *Nature* **504**, 101–106 (2013).
32. M. W. Cunningham Jr *et al*., AT1-AA (angiotensin II type 1 receptor agonistic autoantibody) lockade prevents preeclamptic symptoms in placental ischemic rats. *Hypertension* **71**, 886–893 (2018).
33. A. Hall, L. W. Busse, M. Ostermann, Angiotensin in critical care. *Crit. Care* **22**, 69 (2018).
34. A. Khanna *et al*.; ATHOS-3 Investigators, Angiotensin II for the treatment of vasodilatory shock. *N. Engl. J. Med.* **377**, 419–430 (2017).
35. J. M. Mejia-Vilet *et al*., Angiotensin II receptor agonist antibodies are associated with microvascular damage in lupus nephritis. *Lupus* **29**, 371–378 (2020).
36. C. Sabbadin *et al*., Evaluation of angiotensin II type-1 receptor antibodies in primary aldosteronism and further considerations about their possible pathogenetic role. *J. Clin. Hypertens. (Greenwich)* **20**, 1313–1318 (2018).
37. Anonymous, *Glide; Schrödinger Release 2018-1* (Schrödinger, LLC, New York, 2018).
38. E. Harder *et al*., OPLS3: A force field providing broad coverage of drug-like small molecules and proteins. *J. Chem. Theory Comput.* **12**, 281–296 (2016).
39. M. P. Jacobson *et al*., A hierarchical approach to all-atom protein loop prediction. *Proteins* **55**, 351–367 (2004).
40. Anonymous, *Schrödinger Release 2018-1: LigPrep* (Schrödinger, LLC, New York, 2018).
41. K. D. Singh, K. Muthusamy, Molecular modeling, quantum polarized ligand docking and structure-based 3D-QSAR analysis of the imidazole series as dual AT(1) and ET(A) receptor antagonists. *Acta Pharmacol. Sin.* **34**, 1592–1606 (2013).
42. R. A. Friesner *et al*., Glide: A new approach for rapid, accurate docking and scoring. 1. Method and assessment of docking accuracy. *J. Med. Chem.* **47**, 1739–1749 (2004).
43. R. A. Friesner *et al*., Extra precision glide: Docking and scoring incorporating a model of hydrophobic enclosure for protein-ligand complexes. *J. Med. Chem.* **49**, 6177–6196 (2006).
44. T. A. Halgren *et al*., Glide: A new approach for rapid, accurate docking and scoring. 2. Enrichment factors in database screening. *J. Med. Chem.* **47**, 1750–1759 (2004).
45. Anonymous, *Schrödinger Release 2018-1: Prime* (Schrödinger, LLC, New York, 2018).
46. T. Osajima, M. Suzuki, S. Neya, T. Hoshino, Computational and statistical study on the molecular interaction between antigen and antibody. *J. Mol. Graph. Model.* **53**, 128–139 (2014).
47. H. Sun *et al*., Revealing the favorable dissociation pathway of type II kinase inhibitors via enhanced sampling simulations and two-end-state calculations. *Sci. Rep.* **5**, 8457 (2015).
48. L. F. Braganza, D. L. Worcester, Hydrostatic pressure induces hydrocarbon chain interdigitation in single-component phospholipid bilayers. *Biochemistry* **25**, 2591–2596 (1986).
49. J. D. Faraldo-Gómez, G. R. Smith, M. S. Sansom, Setting up and optimization of membrane protein simulations. *Eur. Biophys. J.* **31**, 217–227 (2002).
50. S. N. Chakraborty, L. D. Gelb, A Monte Carlo simulation study of methane clathrate hydrates confined in slit-shaped pores. *J. Phys. Chem. B* **116**, 2183–2197 (2012).
51. D. Y. T. Darden, L. Pedersen, Particle Mesh Ewald: An N log (N) method for Ewald sums in Large Systems. *J. Chem. Phys.* **98**, 10089–10092 (1993).
52. National Research Council, *Guide for the Care and Use of Laboratory Animals* (National Academies Press, Washington, DC, ed. 8, 2011).
53. I. Nemet *et al*., A cardiovascular disease-linked gut microbial metabolite acts via adrenergic receptors. *Cell* **180**, 862–877.e22 (2020).
54. L. J. Albee *et al*., Identification and functional characterization of arginine vasopressin receptor 1A: Atypical chemokine receptor 3 heteromers in vascular smooth muscle. *Open Biol.* **8**, 170207 (2018).
55. J. M. Eby *et al*., Functional and structural consequences of chemokine (C-X-C motif) receptor 4 activation with cognate and non-cognate agonists. *Mol. Cell. Biochem.* **434**, 143–151 (2017).